

## Article

# Research on the Effect Characteristics of Free-Tail Layout Parameters on Tail-Sitter VTOL UAVs

Hao Qi <sup>1,2</sup>, Shi-Jie Cao <sup>1,3</sup>, Jia-Yue Wu <sup>1,4</sup>, Yi-Ming Peng <sup>1,2</sup> , Hong Nie <sup>1,2</sup> and Xiao-Hui Wei <sup>1,2,\*</sup>

<sup>1</sup> State Key Laboratory of Mechanics and Control for Aerospace Structures, Nanjing University of Aeronautics and Astronautics, Nanjing 210016, China; qihao2020@nuaa.edu.cn (H.Q.); 16601047773@126.com (S.-J.C.); 18222966067@126.com (J.-Y.W.); yimingpeng@nuaa.edu.cn (Y.-M.P.); hnie@nuaa.edu.cn (H.N.)

<sup>2</sup> Key Laboratory of Fundamental Science for National Defense Advanced Design Technology of Flight Vehicle, Nanjing University of Aeronautics and Astronautics, Nanjing 210016, China

<sup>3</sup> China National Space Science Center, Chinese Academy of Sciences, Beijing 100190, China

<sup>4</sup> School of Automation Science and Electrical Engineering, Beihang University, Beijing 100191, China

\* Correspondence: wei\_xiaohui@nuaa.edu.cn

**Abstract:** The tail-sitter VTOL UAV boasts not only high-speed cruising and air hovering capabilities, but also its unique tail-sitting vertical takeoff and landing and hovering attitude enable aerial operations with an exceptionally small cross-sectional area. This feature effectively broadens the scope of application for the UAV in intelligent agriculture, encompassing tasks such as agricultural inspection, production monitoring, and topographic mapping. Given the necessity for frequent modal transitions, this paper is grounded in a thorough examination of the typical structural characteristics of the tail-sitter VTOL UAV. A comprehensive technical solution for tail-sitter VTOL UAVs, based on the free-tail configuration, is proposed in this paper. The free-tail structure is utilized to address the limitations of traditional tailless layout and fixed landing gear in terms of flight stability and takeoff/landing performance of tail-sitter VTOL UAVs. However, the implementation of this solution necessitates the addition of a new maneuvering unit. Consequently, this paper delves into the aerodynamic coupling characteristics and laws between the layout parameters such as tail number, tail length, and tail area and the tail-sitter VTOL UAV fuselage. To optimize the free-tail configuration, a multi-objective optimization is performed by integrating the overall UAV dynamics, landing dynamics, and modal transition trajectory constraints. The results of stability modeling simulations and flight tests demonstrate that the tail-sitter VTOL UAV equipped with this technical solution exhibits enhanced maneuverability and flight efficiency compared to the conventional tailless layout.

**Keywords:** tail-sitter; VTOL; UAV; landing gear; free-tail; CFD; pneumatic layout



**Citation:** Qi, H.; Cao, S.-J.; Wu, J.-Y.; Peng, Y.-M.; Nie, H.; Wei, X.-H. Research on the Effect Characteristics of Free-Tail Layout Parameters on Tail-Sitter VTOL UAVs. *Agriculture* **2024**, *14*, 472. <https://doi.org/10.3390/agriculture14030472>

Academic Editors: Jiyu Li, Jiating Li and Suiyuan Shen

Received: 25 January 2024

Revised: 12 March 2024

Accepted: 13 March 2024

Published: 15 March 2024



**Copyright:** © 2024 by the authors. Licensee MDPI, Basel, Switzerland. This article is an open access article distributed under the terms and conditions of the Creative Commons Attribution (CC BY) license (<https://creativecommons.org/licenses/by/4.0/>).

## 1. Introduction

In 2003 [1,2], the China Academy of Surveying and Mapping spearheaded the design and completion of the first domestic low-altitude UAV remote sensing monitoring system. This cutting-edge system incorporated a surface array CCD digital camera with exceptionally high-resolution capabilities. The monitoring system boasts three control modes: semi-manual control, autonomous control, and remote control of the UAV. Through aerial surveys conducted by the UAV, it was verified that the system successfully achieved its goal of aerial photography for large-scale topographic maps. The VTOL fixed-wing UAV, known as the Zongheng CW-30 [3], employs an inclined photogrammetric measurement system, with ground resolution surpassing 2 cm for precise 1:500 topographic and cadastral surveys. To validate the system's accuracy, experimental results were compared to measured data obtained from total stations and RTK systems. The findings revealed that utilizing UAVs for topographic surveying fully met the planimetric accuracy requirements of 1:500 topographic maps and elevation accuracy requirements of 1:500 topographic maps. This innovative application has had a positive impact on the development of the industry.

As a crucial development direction for VTOL fixed-wing UAVs, tail-sitter VTOL UAVs [4] possess a unique characteristic of maintaining a fixed thrust direction along the longitudinal axis of the fuselage. This enables them to achieve tail-sitter VTOL, as well as aerial hovering capabilities. Such features not only allow for takeoff and landing within a confined ground area but also enable hovering and shuttle flights in minimal cross-sectional spaces. Consequently, they effectively combine high and low altitudes, as well as land and air operations. This makes tail-sitter VTOL UAVs particularly suitable for agricultural production environments that are challenging to address using traditional models and methods. Their flexible monitoring programs, lower costs, high data acquisition efficiency, timely data coverage over a wide range, and excellent realizability make them ideal for such settings. These include vast plot areas and complex terrains where traditional models and methods struggle due to difficulties in point deployment, aircraft accessibility, and low point density. To further enhance the application ability of tail-sitter VTOL UAVs in the agricultural sector, it is imperative to address their takeoff and landing issues, as well as flight stabilization challenges.

Despite significant research efforts dedicated to the flight mechanics and control of tail-sitter VTOL UAVs since their inception in 1944, comparatively little attention has been paid to their takeoff/landing procedures. This paper presents a comprehensive review of the structural configurations of various tail-sitter VTOL UAV designs, focusing on the tailless wing layout adopted by the widely recognized “Google wing” [5]. This layout integrates the vertical tail and fuselage into a single structure to reduce the center of gravity and cruise aerodynamic drag. However, the absence of a horizontal tail rudder surface poses concerns regarding the aircraft’s handling and stability characteristics. In recent years, various researchers have proposed different solutions to address the challenges associated with the takeoff/landing of tail-sitter VTOL UAVs. As shown in Figure 1, literature [6,7] explored the utilization of strut landing gear, while literature [8–10] investigated the application of adaptive landing legs. Additionally, the “U-Lion” [4] design employed a folding wing takeoff/landing scheme, whereas the “Flex-rotor” [11] concept adopted a one-piece flexible landing gear structure, coupled with an open and merged tail configuration. Furthermore, the “THU-1600” [12] model introduced a controlled forward landing scheme. However, it is noteworthy that these aforementioned schemes primarily focus on optimizing individual aspects of the takeoff/landing process for tail-sitter VTOL UAVs, without adequately considering the overall mission envelope and the need to account for multi-mode performance.

This study presents a solution to address the challenges highlighted in the previous section by harnessing the potential of free-wing technology to optimize the performance of tail-sitter VTOL UAVs. The concept of free wing, initially introduced by Zuck [13] in 1945, involves a longitudinal articulated connection between the wing, fuselage, and tail of the vehicle. The free-wing configuration comprises two distinct components: the free-wing and the free tail. The former corresponds to the main wing, which can be freely tilted in relation to the fuselage, while the latter encompasses the tail wing and its associated connecting structure, which can be actively controlled to cater to the specific requirements of the vehicle’s state.

As a result, the complex aerodynamic interference problem between the tail-sitter VTOL UAV propeller and the wing/free tail is one of the key factors affecting the success of tail-sitter VTOL UAV development. During the cruising phase, the non-uniform phenomena arising from the upwash and downwash effects of the rotor propeller slipstream have a substantial impact on the wing’s incoming flow angle of attack [14]. This, in turn, affects the lift and drag characteristics of the wing, particularly its drag properties [15]. Given the non-uniform nature of the propeller’s slipstream, sophisticated methodologies and tools are required for accurate mathematical modeling of its performance [16], as well as for CFD simulations [17,18]. The wing’s span length, the position of the propeller relative to the wing, and the steering of the propeller all exert notable influences on the aerodynamic performance of the vehicle during cruise. As the wing creates a blocking

effect downstream of the rotor propeller, the aerodynamic performance of the propeller itself also undergoes significant changes [19]. Consequently, investigating the aerodynamic interaction between the rotor propeller and the wing holds immense practical significance for comprehending the laws governing propeller-wing aerodynamic interference and for designing and optimizing the aircraft's aerodynamic layout [20].

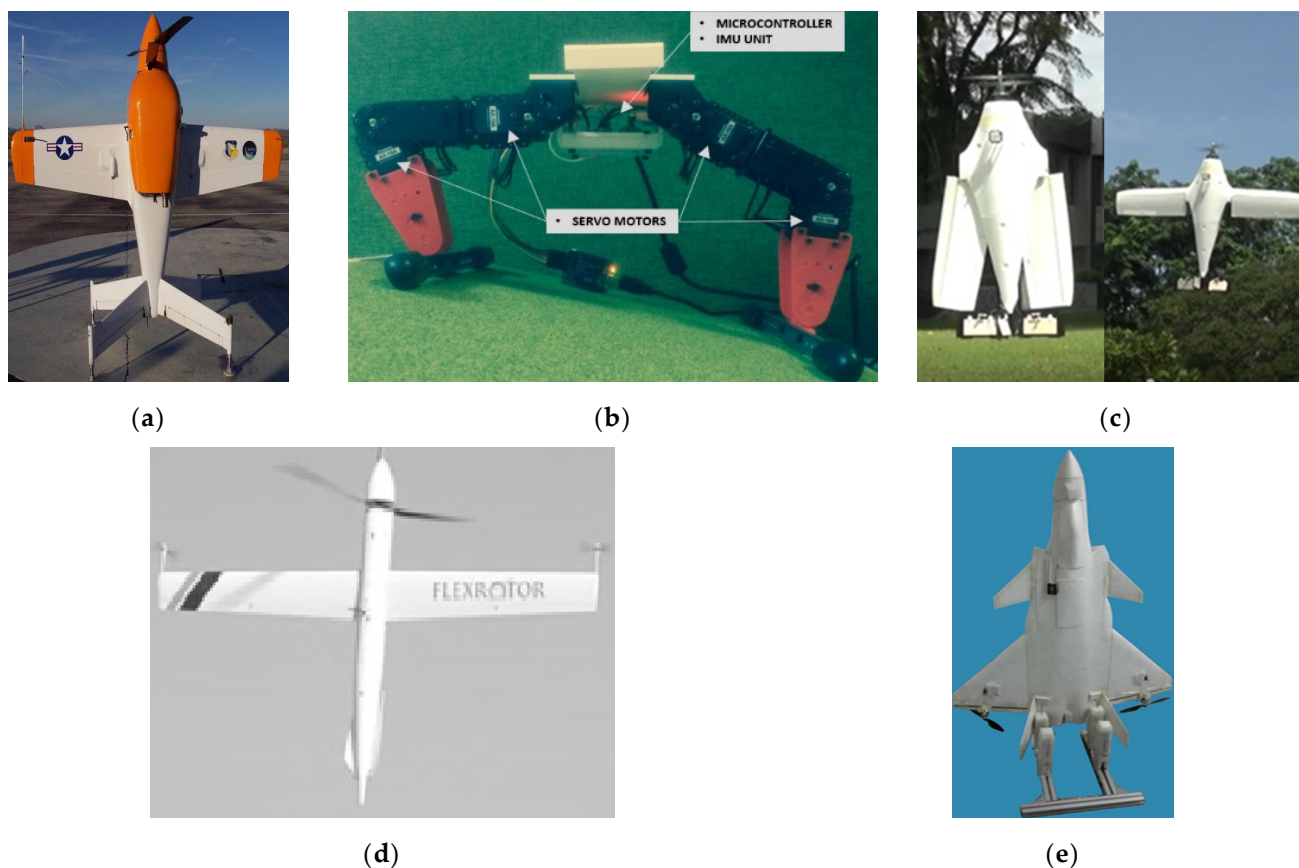


**Figure 1.** Advanced Landing Gear Structural Concept. (a) Strut landing gear; (b) adaptive landing gear; (c) folding wing; (d) flexible landing gear; (e) forward landing.

A significant amount of research has been dedicated to investigating the aerodynamic interference between the propeller and wing in aircraft design. Yang [21] utilized a non-uniform Reynolds-averaged Navier–Stokes equation method, incorporating a dynamic surface lap grid to simulate the interference flow between the propeller slipstream and wing. The study revealed that the presence of the wing disrupted the original periodicity of the propeller slipstream and altered its vortex rotation, consequently affecting the local flow orientation around the wing and its aerodynamic characteristics, particularly at low forward ratios. Sudhakar [22] conducted experimental investigations on the effects of propeller-induced slipstream and vortex fields in a fixed-wing vehicle. Surface oil flow visualization was employed to capture the flow topology on the wing surface under propeller-off and propeller-on conditions. Additionally, the wing/propeller aerodynamic layout was optimized. Zhang [11] analyzed the aerodynamic characteristics of various tandem wing configurations at low Reynolds numbers. This included a tandem wing vehicle with the front wing in both up and down orientations, as well as an inverse tandem wing on the rear wing.

To address the challenges associated with landing and cruising, a folding and retracting free tail of the tail-sitter VTOL UAV is incorporated into the. This active folding and retracting feature enables the wing to reduce the additional drag caused by its structure during cruise mode. For the tail-sitter VTOL UAV, a symmetrical two-segment controllable

free tail is employed, which can be spread to both sides. This configuration assists in enhancing the aircraft's stability in the vertical state. Moreover, the free tail is designed to enable adaptive landings in complex environments, making it well-suited to be applied to agricultural tasks represented by remote sensing. The installation layout of the free tail can be observed in Figure 2. Enhanced flight performance and terrain adaptive takeoff and landing capabilities are essential for the successful implementation of tail-sitter VTOL UAVs in agricultural applications. With this in mind, the current research endeavor aims to: 1. A numerical simulation method applicable to the whole-body interference flow field and aerodynamic characteristics calculation of tail-sitter VTOL UAVs under various conditions has been constructed. The interference flow fields of tail-sitter VTOL UAVs in different flight conditions were simulated, revealing their flow field coupling characteristics, and the influence of free-tail layout parameters on flight performance was analyzed. 2. Based on the influence characteristics of the free tail, its structural parameters under multiple modalities were multi-objectively optimized to achieve the best flight effect. 3. A test prototype of the tail-sitter VTOL UAV was built, and flight tests were conducted to verify that the tail-sitter VTOL UAV optimized through this research with the free tail showed significant performance advantages.



**Figure 2.** Conceptual diagram of the free tail for tail-sitter VTOL UAVs in cruise and takeoff/landing states. (a) Tail-sitter VTOL UAVs in cruise state; (b) Tail-sitter VTOL UAVs in takeoff/landing state.

## 2. Technical Characteristics of Tail-Sitter VTOL UAV with Free-Tail

In the agricultural remote sensing flight envelope and mission profile of a tail-sitter VTOL UAV, a specific sequence of maneuvers is necessary to ensure successful landing in the designated area. This involves adjusting the aircraft's attitude to a vertical upward position before initiating the descent to the desired altitude, ultimately transitioning into a hovering attitude for the final landing. Consequently, the layout design of a tail-sitter VTOL UAV must carefully consider the requirements for both vertical and cruising modes of operation. This adaptation is crucial to ensure optimal performance and seamless transitions between flight phases.

The present study focuses on investigating the impact of free-tail layout parameters on the flight performance characteristics of tail-sitter VTOL UAVs. Previous research conducted by NASA and the Freewing Aircraft Corporation has highlighted the use of double tail spars in free-wing aircraft to enhance structural efficiency and reduce weight [23–25]. Through a comprehensive review of the literature, it has been demonstrated that an elastic aircraft with a higher longitudinal bending stiffness of the tail spar exhibits a reduced induced drag coefficient, leveling rudder deflection coefficient, and overall aircraft drag coefficient. However, as the flight speed increases, the longitudinal bending stiffness of the tail spar decreases, resulting in a rapid decline in elevator maneuvering efficiency and a subsequent fluctuation in the induced drag coefficient of the entire aircraft. Furthermore, by considering the coupled elastic deformation of the tail spar and wing, increasing the longitudinal bending stiffness of the tail spar can enhance the stability of the entire aircraft and improve the efficiency of each maneuvering surface.

During the cruise phase of remote sensing operations, achieving longitudinal trim of the tail-sitter VTOL UAV poses increased challenges due to the absence of a horizontal tail configuration [26]. This is primarily attributed to the vehicle's static stable layout, where the generation of negative lift by the horizontal tail is typically required to maintain the desired angle of approach. Considering the structural efficiency, longitudinal stability, load distribution, lift-to-drag ratio, and versatility in center of gravity placement, the dual tail spar layout proves to be a favorable aerodynamic layout optimization solution for the tail-sitter VTOL UAV.

A comprehensive evaluation of the overall aerodynamic performance of the tail-sitter VTOL UAV with and without free-tail technology was conducted, and the results are illustrated in Figure 3. The integration of free-tail technology confers several benefits. Firstly, the elongated force arm for leveling and maneuvering augments the vehicle's control prowess. Secondly, the minimal additional drag experienced during the leveling process is primarily attributable to the free-tail body's placement at the rear of the fuselage, far from the aircraft's center of gravity. This configuration contributes to enhanced flight efficiency. Moreover, the increase in leveling drag is relatively modest. This technology helps to improve the capability and efficiency of tail-sitter VTOL UAV remote sensing operations in agriculture.

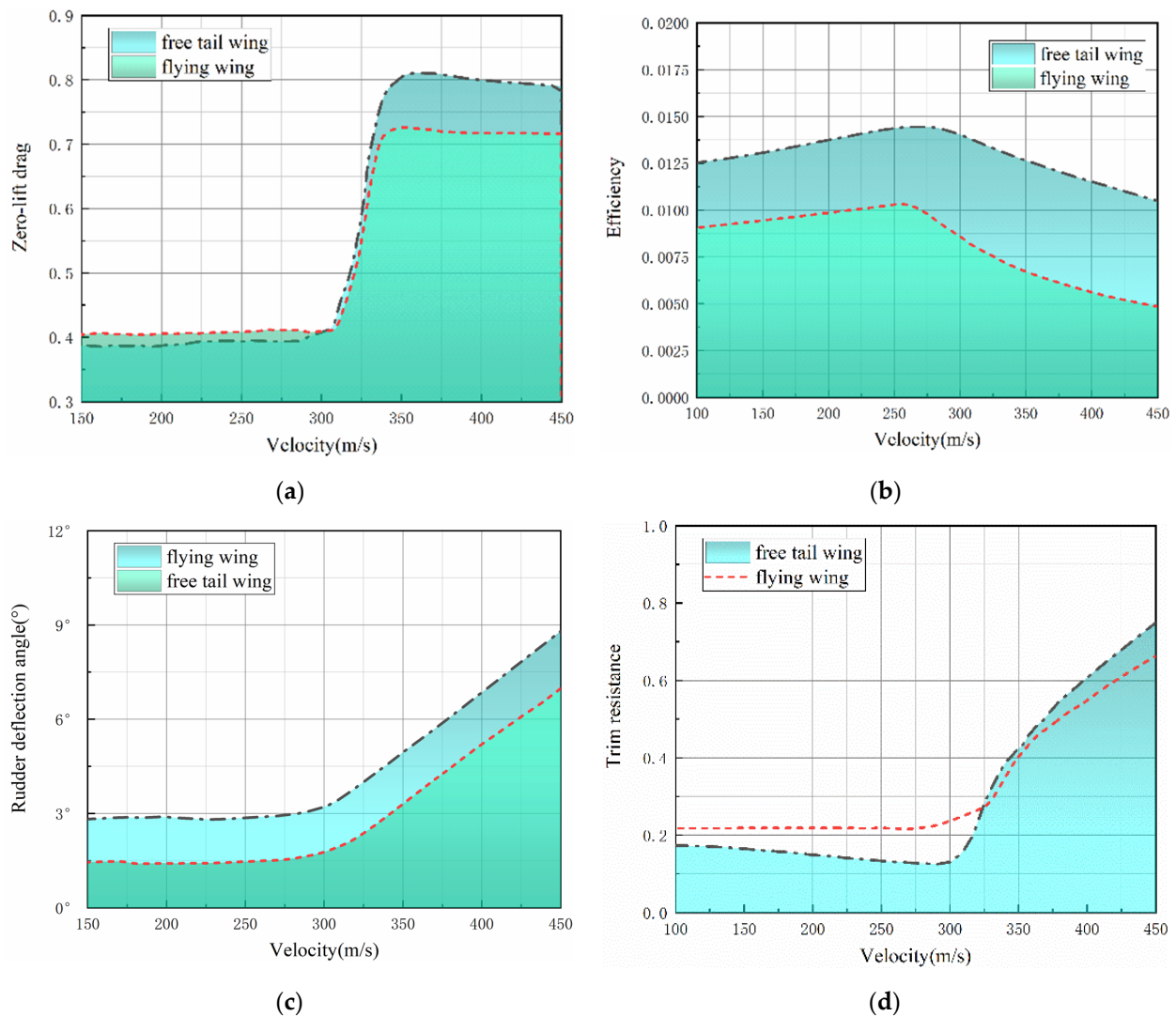


**Figure 3.** Comparison with or without a free tail at the same overload condition. (a) Zero lift drag; (b) rudder surface efficiency; (c) rudder deflection angle; (d) trim resistance.

### 3. Validation of Calculation Method

#### 3.1. Calculation Method and Boundary Conditions

The turbulence model used in this paper is the two-equation SST (Shear Stress Transport)  $k$ - $\omega$  model. The SST  $k$ - $\omega$  model has high accuracy for the calculation of the onset and intensity of flow separation under negative pressure gradient conditions. SST  $k$ - $\omega$  model is a combination of  $k$ - $\omega$  and  $k$ - $\epsilon$  models, and  $k$ - $\omega$  model is used in the boundary layer region and  $k$ - $\epsilon$  model is used in the region outside the boundary layer. The model equation is shown in the following equation, and the values of the coefficients in the equation are taken from the literature [27].

$$\frac{\partial k}{\partial t} + u_j \frac{\partial k}{\partial x_j} = \frac{1}{\rho} \frac{\partial}{\partial x_j} \left[ \left( \mu + \frac{\mu_T}{\sigma_k} \right) \frac{\partial k}{\partial x_j} \right] \left( \frac{Ma_\infty}{Re} \right) + \frac{1}{\rho} P_k \left( \frac{Ma_\infty}{Re} \right) - \beta' \omega k \left( \frac{Re}{Ma_\infty} \right)$$

$$\frac{\partial \omega}{\partial t} + u_j \frac{\partial \omega}{\partial x_j} = \frac{1}{\rho} \frac{\partial}{\partial x_j} \left[ \left( \mu + \frac{\mu_T}{\sigma_\omega} \right) \frac{\partial \omega}{\partial x_j} \right] \left( \frac{Ma_\infty}{Re} \right) + \frac{1}{\rho} P_\omega \left( \frac{Ma_\infty}{Re} \right) - \beta \omega^2 \left( \frac{Re}{Ma_\infty} \right) + 2(1-F) \frac{1}{\sigma_{\omega_2}} \frac{1}{\omega} \frac{\partial k}{\partial x_j} \frac{\partial \omega}{\partial x_j} \left( \frac{Ma_\infty}{Re} \right)$$

In this study, a structured H-H type grid was employed, where the far-field boundary was positioned at 30 times the chord length. The first grid layer's height in the object plane was set to  $1 \times 10^{-6}$  cm. Dimensionless distances, expressed as  $s/c$  and  $g/c$ , were used for computational analysis. When modifying the parameters  $s$  and  $g$ , it was necessary to regenerate the computational grid. To facilitate automatic grid updating in the new configuration, the inverse distance weighting (IDW) method was utilized. IDW is an explicit interpolation algorithm that calculates a weighted average based on the distance between the interpolation point and sample point, which is determined by the following formula:

$$w(x) = \frac{\sum_{i=1}^n v_i \phi(r_i)}{\sum_{i=1}^n \phi(r_i)}$$

where  $w(x)$  is the estimate of the deformation of the grid point  $x = [x \cdot y \cdot z]$ ;  $v_i$  is the known value of the deformation of the  $i$  control point  $x_i = [x_i \cdot y_i \cdot z_i]$ ;  $r_i$  is the Euclidean distance between the grid point  $x$  and the  $i$  control point  $x_i$ , i.e.,  $r_i = \|x - x_i\| \geq 0$ ;  $n$  is the number of control points; the weight function  $\phi(r) = r - q$ , and  $q$  is taken as 3 for the subsequent calculation and analysis.

The deformation mesh generated by the IDW method based on the parameters  $s/c = 2$  and  $g/c = 0$  is shown in Figure 4.

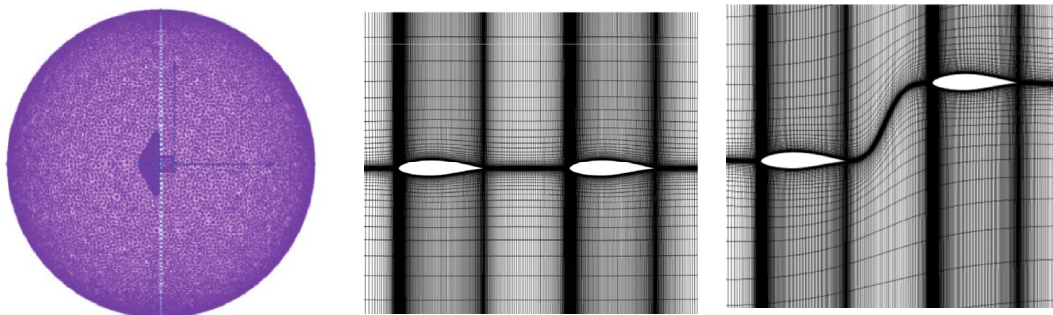


**Figure 4.** CFD calculation grid.

To minimize the impact of grid resolution on calculation accuracy, a grid-independent study was conducted. Five sets of grids with varying sparsity were established, with grid sizes of 550,000, 1.02 million, 2.37 million, 5.92 million, and 8.17 million. The results indicate that the tensile force coefficient decreases with an increase in the advance ratio across

different grid densities. When the advance ratio is held constant, the tension coefficient shows a slight increase with increasing grid volume. However, as the grid volume increases, the differences in calculation results due to grid density gradually decrease. From a grid size of 550,000 to 8.17 million, the computed tail flight efficiency difference decreases gradually. Notably, the efficiencies obtained with grid sizes of 5.92 million and 8.17 million are nearly identical, indicating that the grid size of 5.92 million satisfies the requirement of grid independence. Consequently, the CFD calculations using a grid size of 5.92 million were selected for subsequent comparison and analysis.

Fluent 18.1 was primarily used as the computational software, and its performance was compared with CFX software. Fluent 18.1 employs a finite volume method to discretize the control equations, which ensures better conservation of quantities. The convection term is treated using the high-order accuracy Roe flux difference splitting format, while the diffusion term is discretized using the second-order central difference format. The control equations are solved using the double time step propulsion method. The physical time step is carefully chosen to maintain a Courant number below 5.0, and it is set to approximately 5% of the propeller rotation period for the calculations in this paper. The turbulence is modeled as SST  $k-\omega$ .

The boundary conditions examined in this study are primarily categorized into incoming flow conditions, far-field conditions, solid-wall boundary conditions, and symmetric boundary conditions. The incoming flow is determined by the total temperature, pressure, and flow direction based on the flight altitude and speed. The computational domain's inlet employs a velocity inlet boundary condition, while its outlet utilizes a pressure far-field boundary condition. The far-field boundary employs a reflection-free boundary condition based on the Riemann invariant. The wing, propeller, and hub surfaces are modeled as no-slip adiabatic wall conditions, while the symmetric boundary condition is applied in the computational symmetry plane. The initial field for non-constant calculations is set to achieve a convergent solution for constant calculations.

The pressure-velocity coupling solver utilized is SIM-PLE, and the spatial discretization method employed is second-order upwind format. Gravity is directed downward perpendicular to the entrance velocity, with a gravitational acceleration of  $9.8066 \text{ m/s}^2$ , air density of  $1.225 \text{ kg/m}^3$ , air viscosity of  $1.789 \times 10^{-5} \text{ Pa}\cdot\text{s}$ , and the moment point situated at the center of gravity of the UAV.

### 3.2. Calculation Method Validation

Following a comprehensive analysis of a range of typical tail-sitter VTOL UAV designs, such as the "Sky-Tote", "XFY-1", "VD-200", "T-wing" [28], the present study has determined the optimal conventional maneuvering layout, as illustrated in Figure 5.

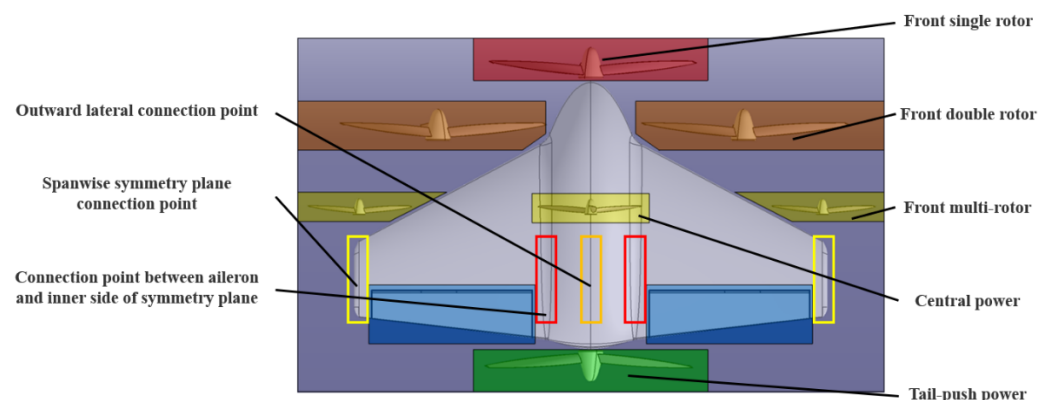


**Figure 5.** Tail-sitter VTOL UAV conventional maneuvering layout scheme.

This study employs a widely adopted flying wing fuselage layout and evaluates various power system configurations for the tail-sitter VTOL UAV, encompassing single,

dual, and multi-power front pull configurations. The primary objective of this assessment is to compare lift ratios and longitudinal maneuvering stability, as depicted in Figure 6. The findings reveal that the front dual power front pull layout at the fuselage yields the highest average lift-to-drag ratio and the least fluctuation in maneuvering moment across varying angles of attack. Consequently, this layout was selected as the power system configuration of agricultural remote sensing tail-sitter VTOL UAVs for further investigation.

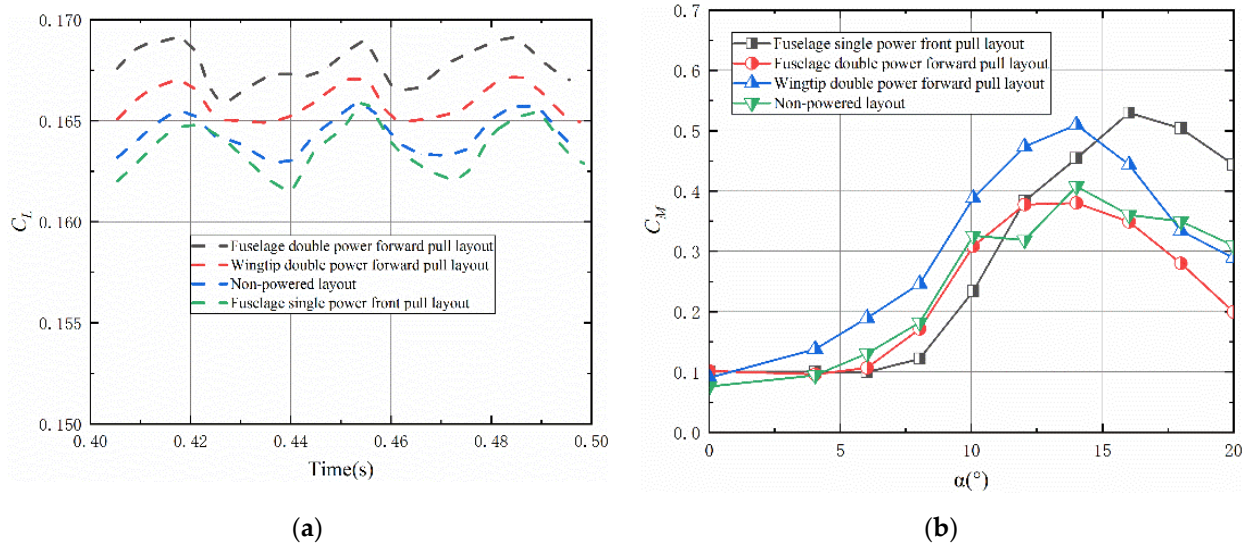


**Figure 6.** Comparison of power layout. (a) Variation in wing lift coefficient  $C_L$  with time; (b) power layout longitudinal maneuvering stability.

In order to verify the accuracy and reliability of the calculation method, this paper first calculates the Graupner E-prop propeller in the literature [29,30] and compares and analyzes it with the experimental results. The Graupner E-prop propeller is a 22.86 cm two-bladed fixed-pitch propeller for multi-rotor aircraft. The experimental and calculation conditions are as follows: height of 0 m, rotational speed of 2500 r/min, incoming flow velocity of 9 m/s, airflow angle normal to the propeller disk of  $0^\circ$ ,  $30^\circ$  and  $60^\circ$ . and the forward ratio  $J$  is 0.32. The geometrical model and results of the experimental values of the propeller pull coefficient  $C_T$  and power coefficient  $C_P$  and the calculated values in this investigation are shown in Figure 7. The comparison revealed that the accuracy of the calculation method and grid utilized in this research is higher than that of the experimental results.

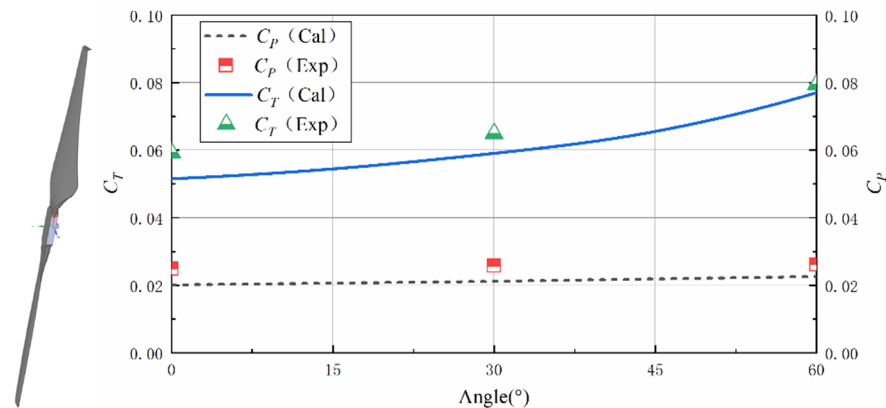


**Figure 7.** Graupner E-prop propeller model and comparison of calculated and tested values.

#### 4. Analysis of the Effect of Free-Tail Layout Parameters of Remote Sensing Tail-Sitter VTOL UAV in Cruise Mode

The parameters of the remote sensing tail-seat VTOL drone prototype used in this study are shown in Table 1.

**Table 1.** Remote sensing Tail-sitter VTOL UAV parameters.

Design Entry	Parameters
Takeoff weight	1 kg
Cruise Speed	25 m/s
Wingspan	0.92 m
Surface area of wing	0.17 m <sup>2</sup>
Propeller disc radius	0.18 m
Average aerodynamic chord length	0.15 m
Single elevator area	0.06 m <sup>2</sup>
Maximum thrust per propeller	10 N
Maximum elevator and rudder deflection angle	30°
Maximum elevator and rudder deflection rate	120°/s
Maximum propeller thrust change rate	20 N/s
Payload	200 g
Endurance	20 min

##### 4.1. Analysis of the Influence of the Free-Tail Installation Position of Remote Sensing Tail-Sitter VTOL UAV in Cruise Mode

In the context of the free-tail layout of the tail-sitter VTOL UAV, the selection of layout can be determined based on the installation position. Three options are considered: the aileron inboard connected double tail spar layout, the wingtip connected double tail spar layout, and the fuselage axis connected single tail spar layout.

This paper focuses on analyzing the aerodynamic characteristics of the aileron inboard connection double tail spar layout. At this cruise state, the rotor propeller advance ratio is 3.12, the Reynolds number  $\approx 20,000$ , and the incoming Mach number  $Ma$  is 0.124. Figure 8 illustrates that the primary factor affecting the flat tail is the presence of a strong downwash region on the inner side.

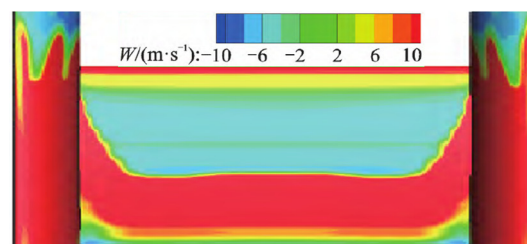


**Figure 8.** Vortex cloud around the tail spar attached to the inner aileron.

The downwash gradient consistently exhibits a negative value, primarily concentrated above the flat tail at a small angle of attack. As the angle of attack increases, the strong downwash area gradually moves away from the flat tail. This behavior can be attributed to the right flat tail being positioned upstream of the upstream propeller, thus experiencing the upwash effect from the propeller. Consequently, the flat tail exhibits a higher angle of attack, and the central area of its strong downwash region remains elevated.

Secondly, the wingtip is connected to the double tail spar layout due to the wingtip vortex generated by flow separation on the wing, as well as the coupling effect of the vortex system structure on the tail. This coupling effect significantly reduces the lift provided by the free tail. Moreover, when the wingspan is too large, the stiffness of the free tail decreases. Consequently, at the same flight speed, the induced drag produced by the flat tail increases as the stiffness of the tail spar decreases due to higher flight dynamic

pressure. The elasticity of the tail brace structure also affects rudder maneuvering efficiency, with a decrease in efficiency as tail brace stiffness decreases. This decrease occurs more rapidly with lower tail brace stiffness, necessitating an increase in rudder deflection angle to achieve pitch balance.

Finally, when the angle of attack  $\alpha$  is  $0^\circ$ , the fuselage axis is connected to the single tail spar layout. The tail contraction of the actual rear body shape creates a large low-pressure region in the tail. However, the presence of the tail spar disrupts this tail contraction, causing the original low-pressure area to vanish and resulting in an increase in pressure on the upper surface of the airfoil, which leads to a decrease in lift coefficient. Additionally, the expansion of the rear body and the presence of the tail spar cause pressure in the vicinity of the tail spar to decrease, leading to a reduction in drag coefficient. The pressure on the upper surface of the airfoil in the tail section of the wing is located behind the center of mass, generating an additional nose-up moment. When  $\alpha$  is  $36^\circ$ , the tail section becomes a relatively high-pressure region without a tail spar, and the presence of the tail spar causes a decrease in pressure on the upper airfoil surface of the tail, resulting in an increase in lift coefficient and generating an additional nose-down moment.

Based on these findings, this paper recommends the aileron inboard attached double tail spar layout as the preferred mounting configuration for remote sensing tail-sitter VTOL UAVs equipped with free-tail fins.

#### 4.2. Analysis of the Influence of Free-Tail Length Parameters of Remote Sensing Tail-Sitter VTOL UAV in Cruise Mode

According to the horizontal tail efficiency calculation equation:

$$C_{mH} = k_q C_{L\alpha H} [(1 - \varepsilon_\alpha)\alpha + \delta_H] \frac{S_H l_H}{S C_A}$$

The horizontal tail efficiency is related to the geometric parameters such as tail force arm  $l_H$  and horizontal tail area  $S_H$ .

To attain optimal aerodynamic performance of the free-tail layout, it is crucial to consider the intricate aerodynamic interactions between the free tail and the wing, as well as the maneuverability of the horizontal tail. In this study, we replace the conventional T-tail with a direct arrangement of the horizontal tail behind the wing and investigate the aerodynamic interference characteristics of the double tail spar layout under cruise conditions. The analysis takes into account variations in the installation position and structural length of the free tail, while also considering the 3D effects of finite wingspan. Figure 9 provides a visualization of the free-tail/wing position relationship and the corresponding grid.

When considering the length of the free tail, it is essential to take into account the spacing between the horizontal tail and the wing. Figure 10 provides a visual representation of this relationship.

Placing the horizontal tail too close to the wing can result in the formation of a vortex behind the wing due to the convergence of air with varying flow directions along the upper and lower surfaces of the wing. Additionally, the propeller slipstream can amplify the size of this vortex, leading to a significant increase in instantaneous acceleration. Moreover, the propeller tip vortex continues to exert a strong influence even after passing the lower surface of the wing, causing an irregular distribution of the flow field at the trailing edge of the wing. On the other hand, positioning the horizontal tail too far away from the wing reduces the coupling effect and effectively avoids the rotational slipstream. However, excessively increasing the distance can impact the takeoff/landing of the tail-sitter VTOL UAV by affecting the center of gravity height. Furthermore, it reduces the stiffness of the free tail and increases the complexity of the structural design. Therefore, determining the optimal length of the free tail requires careful consideration and balance of these factors.

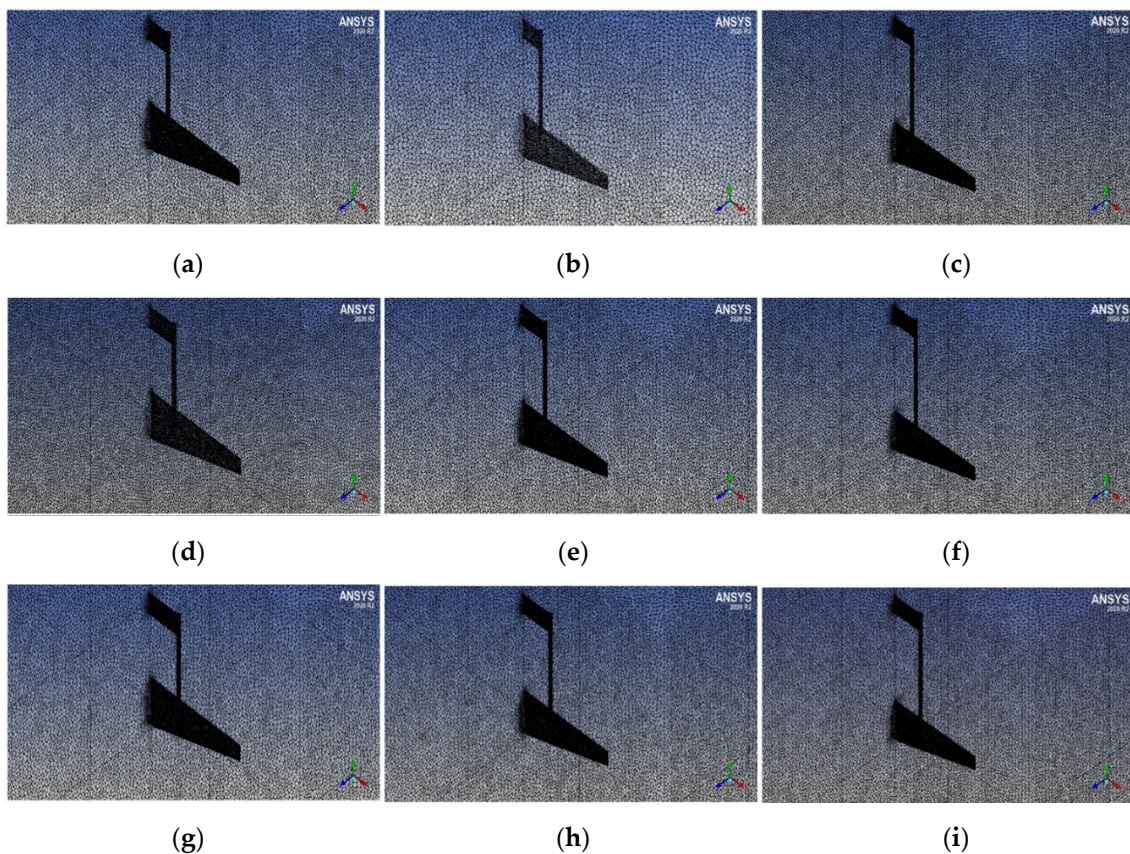


**Figure 9.** Position relationship and mesh of free-tail/wing in cruise state. (a) Width 200, Length 400; (b) Width 200, Length 500; (c) Width 200, Length 600; (d) Width 250, Length 400; (e) Width 250, Length 500; (f) Width 250, Length 600; (g) Width 200, Length 400; (h) Width 200, Length 500; (i) Width 200, Length 600.

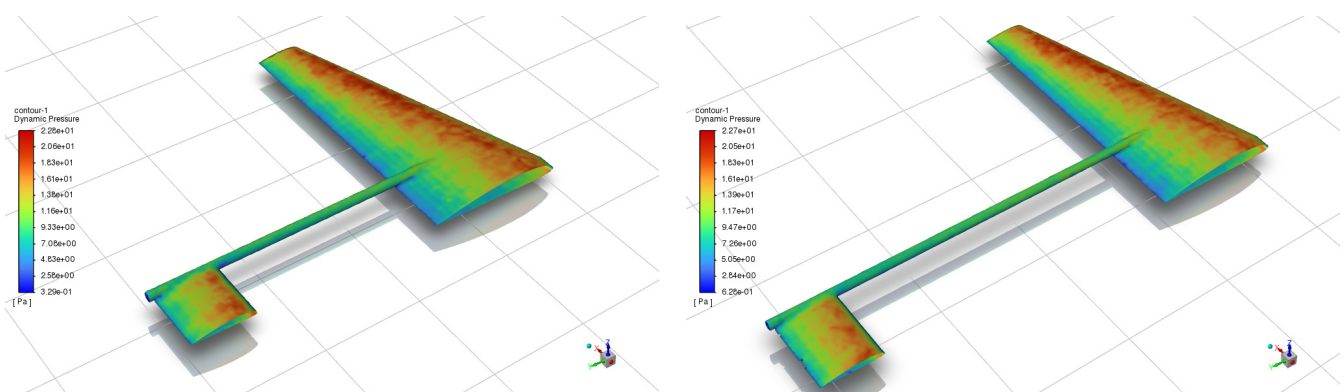


**Figure 10.** Characteristics of free-tail length parameters on horizontal tail aerodynamic effects.

Simulation tests were conducted by modifying the free-tail length in both directions, using the fuselage length as the reference point. Given the low-speed characteristics of the verification aircraft developed in this research, the aerodynamic coefficient is primarily affected by the rudder surface and the angle of attack. Hence, the main performance metric considered is the lift-to-drag ratio of the horizontal tail. The results are presented in Figure 11. Based on the findings, it is recommended that the free-tail length should not be excessively short and can be comparable to or slightly longer than the fuselage length.

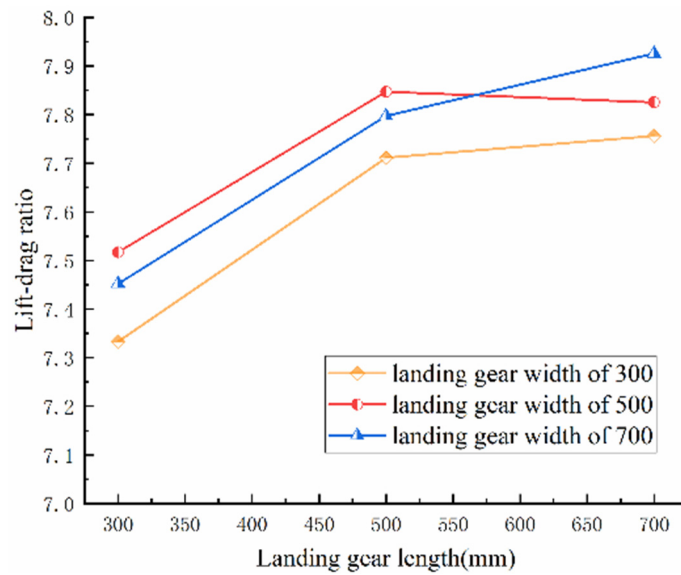


**Figure 11.** Horizontal tail lift to drag ratio with different free-tail parameters.

*4.3. Analysis of the Influence of Free-Tail Orientation Parameters of Remote Sensing Tail-Sitter VTOL UAV in Cruise Mode*

As depicted in Figure 12, when the free tail is at a small attack angle, the downwash flow from the front rotor impacts the middle section of the free tail near the wing root, resulting in the formation of a downwash vortex on the horizontal tail surface. Simultaneously, the upwash vortex deflects upward, leading to a decrease in the effective angle of attack and lift. As the angle of attack increases, the airflow produced by the propeller deviates towards the fuselage, and the rotor downwash flow passes over the upper surface of the free-tail root, effectively preventing airflow separation. This results in increased lift. However, similar to the front wing, airflow separation occurs in the middle of the trailing edge of the free tail at larger angles of attack, causing a reduction in free-tail lift. The clean configuration of the free-tail root experiences significant stall under high angles of attack. Nevertheless, in the forward pull layout, the slipstream from the rotor effectively alleviates the stall at the free-tail root, thereby increasing lift.

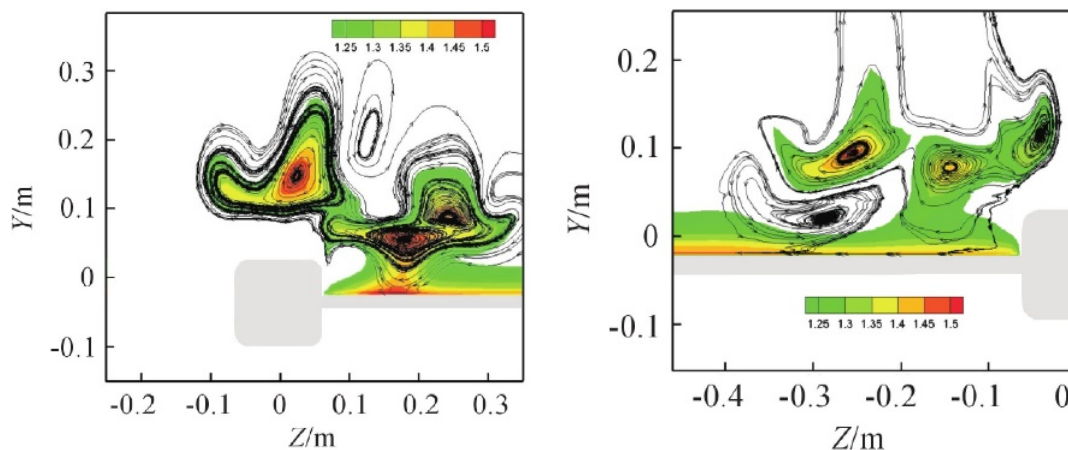


**Figure 12.** Free-tail vortex structure cloud diagram.

As the free-tail span parameter and the relative position with the propeller are varied, the free-tail lift exhibits an initial increase, followed by a decrease, and eventually stabilizes, as demonstrated in Figure 13. Similar to the observed trend in lift, changes in drag are predominantly concentrated near the propeller hub. An increase in the axial induced speed

and effective angle of attack on the upper wash side contributes to a reduction in differential pressure drag. Conversely, the lower wash side experiences an increase in friction drag due to the increased axial induced speed. However, this increase in friction drag also helps mitigate the rise in differential pressure drag, resulting in a smaller overall increase in drag compared to the decrease in drag on the upper wash side. Consequently, the overall drag is reduced, leading to an improvement in the lift-to-drag ratio of the wing section.

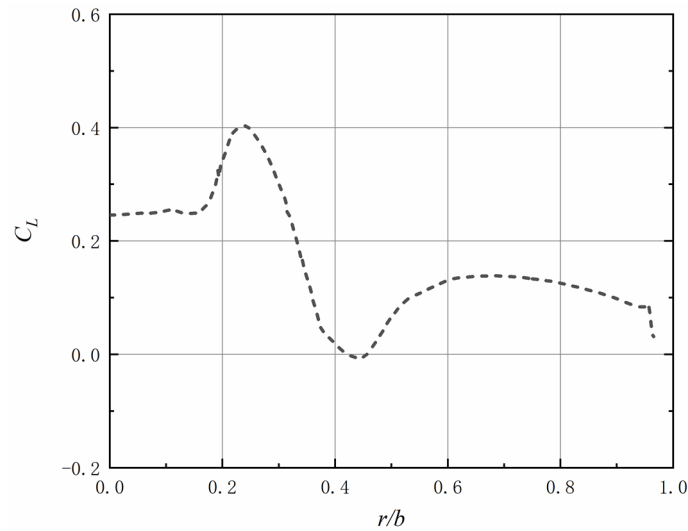


**Figure 13.** Flat tail spread lift distribution.

*4.4. Analysis of the Influence of the Number of Free-Tail Fins of Remote Sensing Tail-Sitter VTOL UAV in Cruise Mode*

As shown in Figure 14, the stall angle of welcome for both biplane layouts is greater than that of the monoplane.

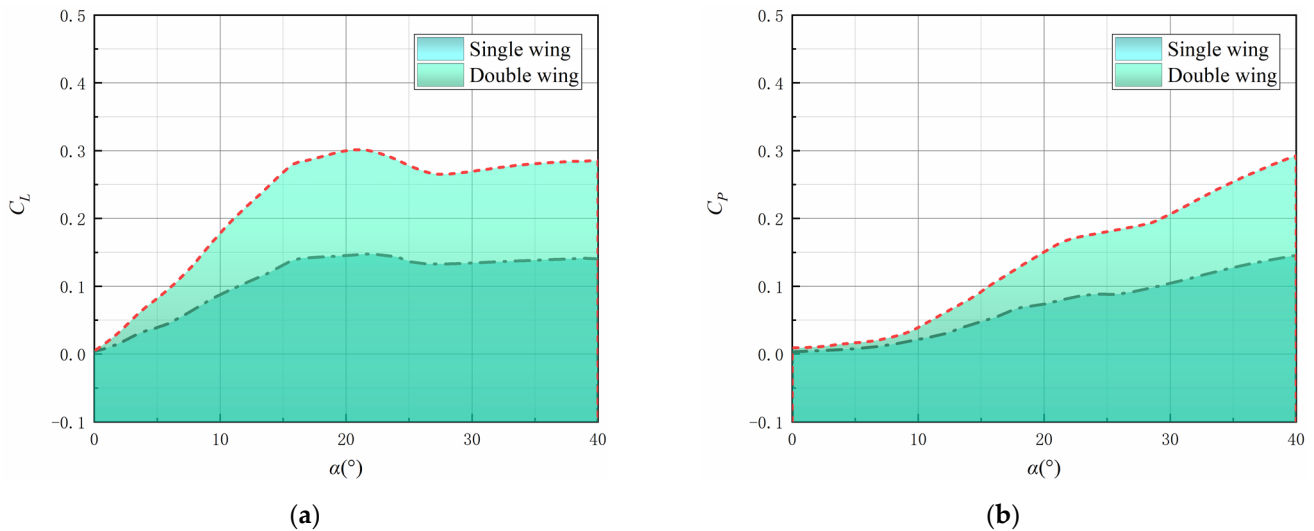


**Figure 14.** Single and double wing layout lift drag comparison. (a)  $C_L$ ; (b)  $C_D$ .

The reduction in the effective angle of the biplane due to the down washing of the upper and lower wings is the reason for the lower lift to drag ratio of the biplane compared to the monoplane at varying degrees. This effect is attributed to the unfavorable induction and interference between the biplane wings. However, the lift and drag of the biplane are higher than those of the monoplane at the same angle, indicating that the influence of induction and interference between the biplane wings is favorable at this spacing. This is because the development of the leading edge vortex and tip vortex of the lower wing is

suppressed by the upper wing, thereby reducing the three dimensional non-linear lift and total lift of the biplane. The reduction in induced drag is advantageous and keeps the total drag from becoming too large. At an increasing angle of attack, the pressure center of both the monoplane and the biplane moves downstream. The pressure center of the biplane is positioned in front of the monoplane since the compression of the upper wing makes the low pressure area formed on the upper surface of the lower wing by the leading edge vortex and the wing tip vortex smaller.

### 5. Analysis of the Effect of Remote Sensing Tail-Sitter VTOL UAV Free-Tail Parameters in Transition Mode

When making a transition, a tail-sitter VTOL UAV is subject to multiple constraints that reflect the feasible state space of the UAV in the transition mode:

#### (1) State constraints

The forward transition is described in detail here, and the forward transition is a process of acceleration and head-down, so the combined external force component should satisfy, and the pitch angle velocity should satisfy  $q \leq 0$ . In addition, since the maximum velocity of the prototype is 20 m/s and the maximum rudder deflection angle is  $30^\circ$ , the range of the transition corridor velocity constraints and the constraints of the rudder deflection angle are  $V \in [0, 20]$  and  $\delta_e \in [-30^\circ, 30^\circ]$ , respectively.

#### (2) Angle of approach constraints

The angle of approach has a decisive effect on the aerodynamic force of the UAV. In order to ensure the safety of the transition, the free-zone wing angle constraints during the transition are set as  $\alpha_{out} \in [0, \alpha_{max}]$ ,  $\alpha_{max}$  is the maximum allowable angle, and  $\alpha_{max}$  is usually taken as 80% of the stall angle value in the past experiments.

#### (3) Thrust constraint

The maximum thrust of a single propeller of the prototype in this paper is 10 N, so the total thrust constraint range is:

$$0 \leq F_{T1} + F_{T2} \leq 20$$

In addition, in order to ensure the safety of the transition, it is necessary to ensure that the airplane can not fall high, and at the same time, there can not be too large an increase in altitude.

Therefore, this study sets the altitude change constraints as follows:

$$\begin{cases} F_{e,z}^B \leq 0 \\ -3 \leq \dot{z}^I \leq 0 \end{cases}$$

where  $\dot{z}^I$  is the altitude change rate of the UAV. In summary, the complete set of equations for solving the transition corridor for a tail-sitter VTOL UAV is as follows.

$$\begin{cases} F_{e,x}^B \geq 0 \\ F_{e,z}^B \leq 0 \\ M_{e,\nu}^B = 0 \\ q \leq 0 \\ -3 \leq \dot{z}^I \leq 0 \\ 0 \leq F_{T1} + F_{T2} \leq 20 \\ V \in [0, 20] \\ \delta_e \in [-30^\circ, 30^\circ] \\ \alpha_{out} \in [0, \alpha_{max}] \end{cases}$$

### 6. Analysis of the Effect of Free-Tail Parameters of Remote Sensing Tail-Sitter VTOL UAV in the VTOL Mode

Thrust of the propeller in the hovering state is:

$$f_1^b = (0 \ 0 \ -f_1)^T, f_2^b = (0 \ 0 \ -f_2)^T$$

Gravity is:

$$G^I = (0 \ 0 \ mg)^T$$

The pneumatic power provided by the rudder is:

$$F_{\delta 1}^b = (-L_{\delta 1} \ 0 \ D_{\delta 1})^T, F_{\delta 2}^b = (-L_{\delta 2} \ 0 \ D_{\delta 2})^T$$

Among them:

$$L_{\delta 1} = Q_1 S_{\delta} C_{L_{\delta}} \delta_1, D_{\delta 1} = Q_1 S_{\delta} C_{D_{\delta}} \delta_1$$

$$L_{\delta 2} = Q_2 S_{\delta} C_{L_{\delta}} \delta_2, D_{\delta 2} = Q_2 S_{\delta} C_{D_{\delta}} \delta_2$$

According to momentum theory, the dynamic pressure due to the slipstream at the propeller disc is:

$$Q = \frac{4f}{\pi d}$$

Then, the longitudinal dynamics model of this tail-sitter VTOL UAV during the hover phase is:

$$\begin{cases} I_{yy} \ddot{\theta} = M_{Ty} - L_{ele}(h - h_{ele}) + \Delta M_y \\ m \ddot{x}_{oI} = -(T - D_{ele}) \sin \theta - L_{ele} \cos \theta \\ m \ddot{z}_{oI} = mg - (T - D_{ele}) \cos \theta + L_{ele} \sin \theta \end{cases}$$

In which:

$$L_{ele} = L_{\delta 1} + L_{\delta 2}; D_{ele} = D_{\delta 1} + D_{\delta 2}$$

Refer to Figure 15 for the meaning of the equation symbols and reference coordinate system.

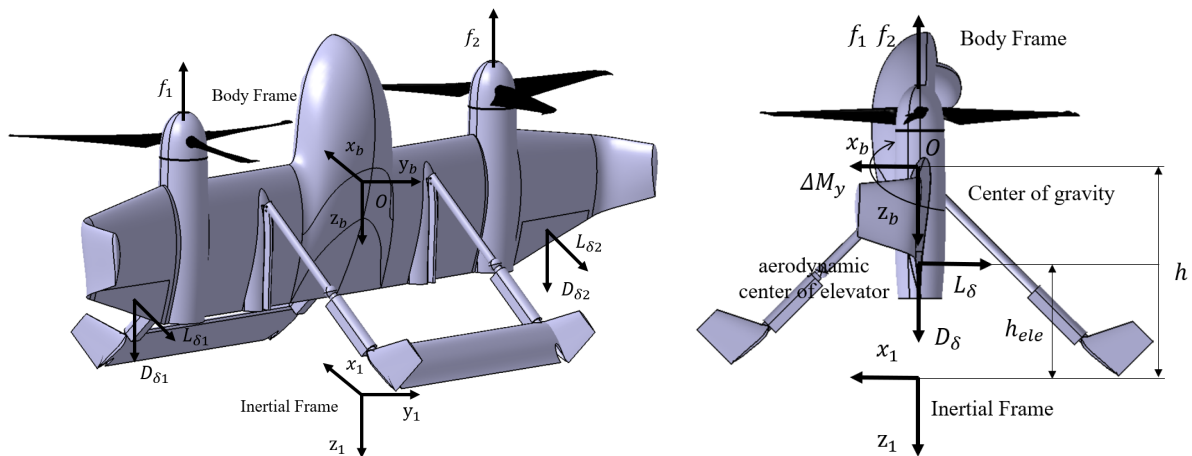


**Figure 15.** Tail-sitter VTOL UAV hover phase coordinate system definition and force analysis.

Figure 16 is a sketch of the force on the landing gear of tail-sitter VTOL UAVs at the touchdown stage, where the force between the ground and the landing gear is relative to the center of gravity to produce moments. As the momentum is generated by the horizontal speed, the component of thrust in the horizontal plane can make the tail-sitter VTOL UAV flip around the landing gear/ground contact point.

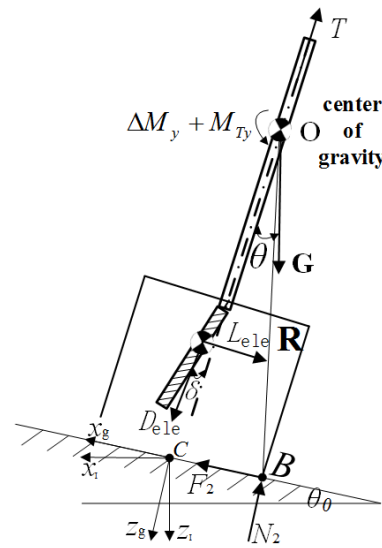


Figure 16. Diagram of tail-sitter VTOL UAV touchdown force analysis.

The ground support and friction forces on the landing gear on each side are:

$$F_A^g = ( 0 \quad -F_1 \quad -N_1 )^T$$

$$F_B^g = ( 0 \quad -F_2 \quad -N_2 )^T$$

At this point, the longitudinal dynamics are:

$$\begin{cases} I_{yy}\ddot{\theta} = \Delta M_y + M_{Ty} - L_{ele}(h - h_{ele}) - N_2|R| \cos(\theta - \theta_0 + \eta_0) + F_2|R| \sin(\theta - \theta_0 + \eta_0) \\ m \begin{pmatrix} \ddot{x}_{og} \\ \ddot{z}_{og} \end{pmatrix} = \begin{pmatrix} F_2 \\ -N_2 \end{pmatrix} + mg \begin{pmatrix} -\sin \theta_0 \\ \cos \theta_0 \end{pmatrix} + \begin{pmatrix} \cos(\theta - \theta_0) & \sin(\theta - \theta_0) \\ -\sin(\theta - \theta_0) & \cos(\theta - \theta_0) \end{pmatrix} \begin{pmatrix} -L_{ele} \\ D_{ele} - T \end{pmatrix} \end{cases}$$

$\theta_0$  is the angle of inclination of the ground,  $|R| = \sqrt{h^2 + a^2}$  is the distance from the aircraft to the ground contact point, and the other terms are:

$$L_{ele} = L_{\delta 1} + L_{\delta 2}; D_{ele} = D_{\delta 1} + D_{\delta 2}; \eta_0 = \arctan(a/h)$$

The overturning moments during the landing phase are:

$$M_y = -mg|R|\sin(\eta_0 - \theta) + (T - D_{ele})a + L_{ele}h_{ele} + M_{Ty} + \Delta M_y$$

The tail-sitter VTOL UAV is dynamically stable when the torque is less than zero. Define the rollover balance angle as  $\eta = \min(\eta_0, \theta_{trim})$ , where  $\theta_{trim}$  is the moment balance angle and  $M_y(\theta_{trim}) = 0$ . When the projection of the center of gravity of the tail-sitter VTOL UAV on the ground exceeds the polygon formed by the touchdown point of its landing gear, the aircraft is statically unstable, and the static stability boundary  $\eta_0$  is defined. Based on this, the following stability margins determined by the flip energy are proposed:

$$S_{LDESM} = E_y / (mg\bar{c})$$

The flip energy is:

$$E_y = mg|R|[\cos(\eta_0 - \eta) - \cos(\eta_0 - \theta)] - (T - D_{ele})a(\eta - \theta) - L_{ele}h_{ele}(\eta - \theta) + \int_{\theta}^{\eta} M_{Ty}(\theta)d\theta$$

As a result, the pitch angle equilibrium points can be obtained for different landing gear length parameters as shown in Figure 17, and the landing gear length parameters can be optimized sequentially.

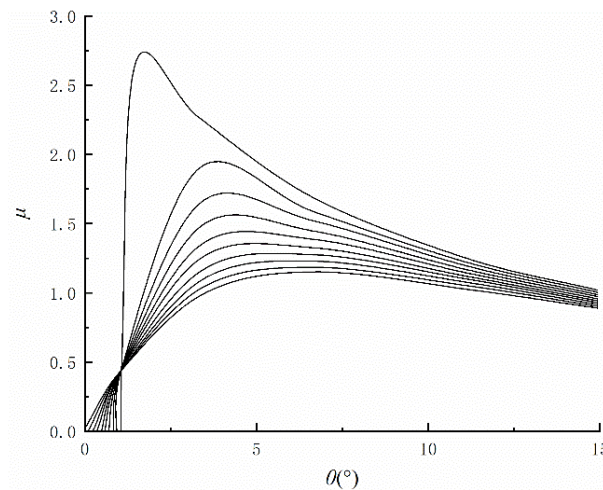


**Figure 17.** Pitch angle equilibrium points for different landing gear length parameters.

In addition, during the VTOL state, the free tail is subject to the influence of the rotor slipstream, which can be attributed to the low relative velocity with the air.

As per the momentum theory, the pull force produced by the rotor can be mathematically described as:

$$T_l = 2\rho A_l (V_\infty + v_{l,0})v_{l,0}$$

where  $V_\infty$  is the incoming velocity,  $A_l$  is the rotor blade area, and  $v_{l,0}$  is the average induced velocity at the rotor blade plane.

$$v_{l,0} = \frac{1}{2} \left( -V_\infty + \sqrt{V_\infty^2 + \frac{2T_l}{\rho A_l}} \right)$$

The relationship between the rotor speed and the average induced velocity at the propeller disc surface is further obtained as:

$$v_{l,0} = \frac{1}{2} \left( -V_\infty + \sqrt{V_\infty^2 + \frac{8C_{Tl}\omega_l^2 D_l^2}{3600\pi}} \right)$$

The average induced velocity on the wing at a distance of  $x_l$  from the plane of the propeller disc is:

$$v_{l,x} = v_{l,0} \left[ 1 + \frac{x_l/R_l}{\sqrt{1 + (x_l/R_l)^2}} \right]$$

Considering the rotor induced velocity, the combined velocity of the airflow in different regions of the wing aerodynamic center is:

$$V_{out} = V = \sqrt{u^2 + w^2}$$

$$V_{in,l} = \sqrt{(u + v_l)^2 + w^2}$$

where  $V_{out}$  is the combined velocity of airflow in the free-flow region,  $V_{in,l}$  is the combined velocity of airflow in the rotor slipstream region,  $u$  is the component of the free-flow velocity in the  $x_b$  axis of the airframe coordinate system,  $w$  is the component of the free flow velocity in the  $z_b$  axis of the airframe coordinate system,  $v_l$  is the rotor induced velocity, and the head on angle of the aerodynamic center of the free flow region can be expressed as:

$$\alpha_{out} = \begin{cases} 0, & u = 0, w = 0 \\ \frac{\pi}{2}, & u = 0, w \neq 0 \\ \arctan\left(\frac{w}{u}\right), & u \neq 0 \end{cases}$$

The head on angle of the aerodynamic center of the rotor slipstream region can be expressed as:

$$\alpha_{in,l} = \arctan\left(\frac{w}{u + v_l}\right)$$

The radius of the corresponding rotor slipstream zone is:

$$R_{l,x} = R_l \sqrt{\frac{v_{l,0}}{v_{l,x}}}$$

It has been observed that as the distance between the wing and the propeller disk increases, the average induced velocity gradually rises while the slipstream radius decreases. To streamline calculations, the average induced velocity at the aerodynamic center of the wing rotor slipstream area is considered instead of the induced velocity of the entire area. By utilizing the radius of the slipstream area at the aerodynamic center and relevant geometric parameters, the areas of different slipstream regions are determined. Additionally, as depicted in Figure 18, Considering that the free tail attitude has a large influence on the slipstream area, the free tail slipstream disturbance characteristics under vertical takeoff and landing are simulated with 5° as a working condition point. Due to the large number of cases, plus the high similarity between the cases, this paper integrates the simulation flow through Insight with the program shown in Figure 19, and the ICEM and Fluent’s Replay, Journal function of ICEM and Fluent for secondary development to realize the transfer of operation files, data collection and automation.

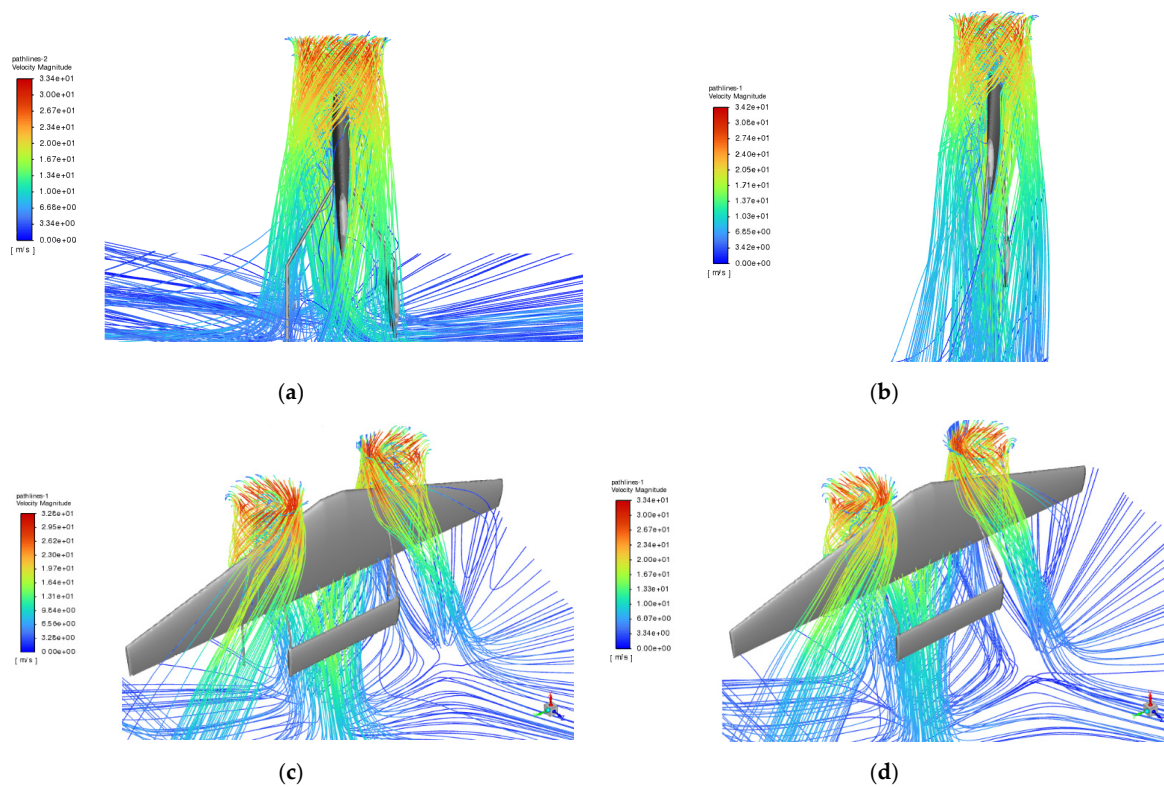


**Figure 18.** Rotor slipstream flow diagram in different free-tail attitudes. (a) Side view with free tail spread 30°; (b) side view with free tail spread 5°; (c) axis side view with free tail spread 15°; (d) axis side view with free tail spread 45°.

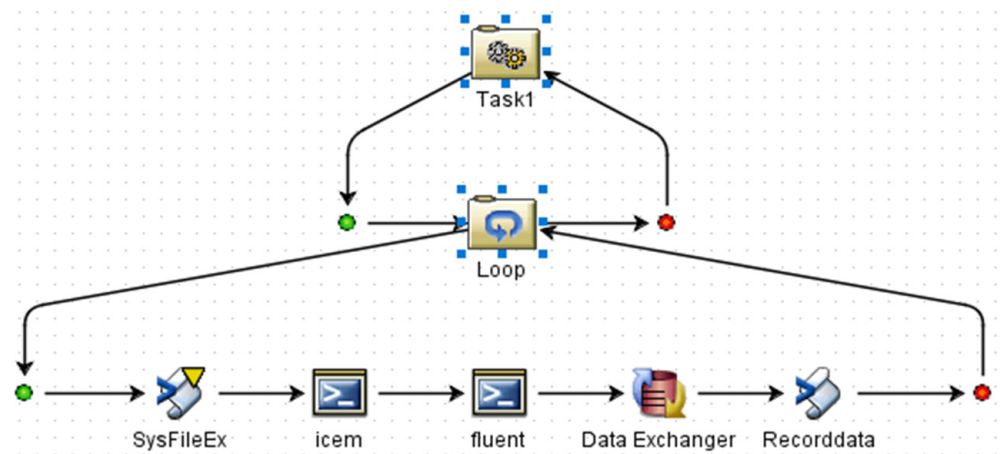


Figure 19. Insight integration flowchart.

The results are presented in Figure 20.

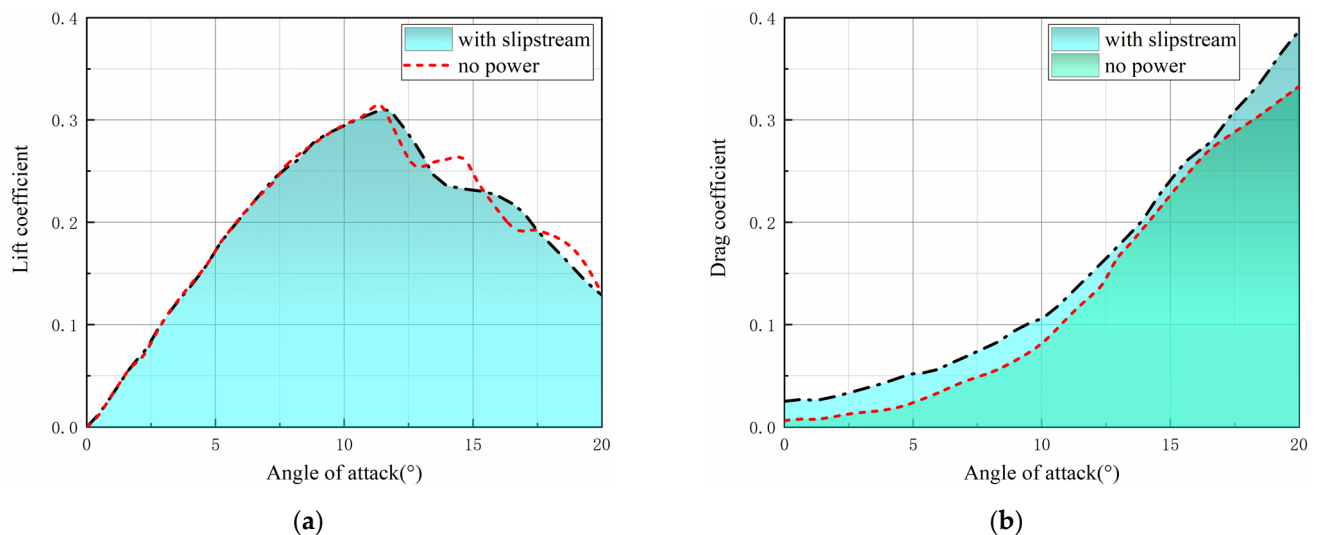
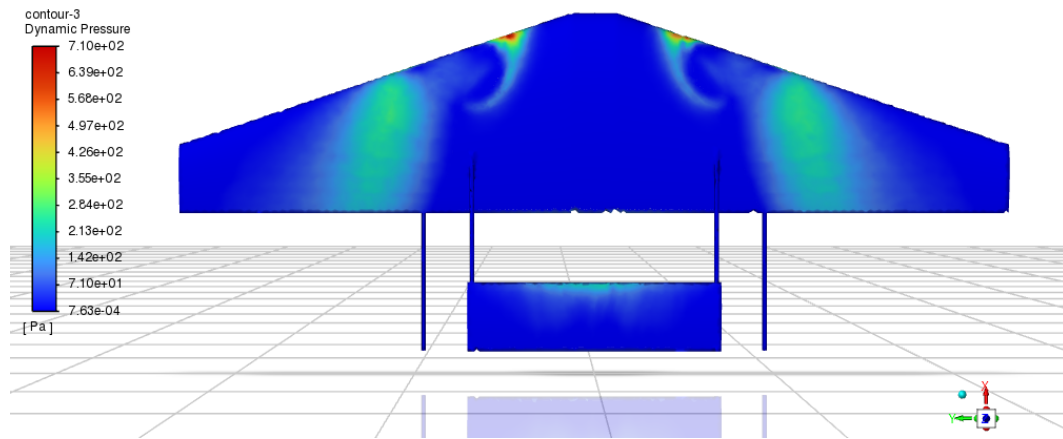


Figure 20. Lift and drag coefficient with or without slipstream. (a) Lift coefficient; (b) drag coefficient.

The computational results demonstrate the influence of the rotating slipstream on the spacing of the free tail, leading to variations in dynamic pressure across the span of the horizontal tail, as shown in Figure 21. This phenomenon occurs due to the disruption of airflow after passing through the wing, resulting in the formation of a stronger vortex on the upper surface of the airfoil. Consequently, the dynamic pressure along the span of the airfoil increases incrementally on the upper surface. Consequently, the static pressure on the horizontal tail surface changes, and when combined with the downwash airflow on the horizontal tail, both the lift and drag coefficients of the horizontal tail decrease, with a more significant reduction in the lift coefficient. As the free-tail spacing exceeds the rotor spacing and continues to increase, a portion of the horizontal tail experiences the influence of the rotating slipstream on the opposite side of the rotor. This alteration affects the effective airflow angle of attack and leads to the deviation of the horizontal tail from its ideal operating condition.

Consequently, the parameters of the free tail in the tail-sitter VTOL UAV during the VTOL mode primarily influence the maneuvering efficiency through attitude control. Hence, the performance in cruise mode can be predominantly assessed.



**Figure 21.** Horizontal trailing edge spreading dynamic pressure distribution.

## 7. Multi-Objective Optimization

### (1) Optimal height change

During the transition phase, the change in altitude is a crucial indicator. Therefore, this paper establishes an optimization objective function for the transition height change as:

$$J_1 = \int_{t_0}^{t_n} (h(\tau) - h_{\text{init}})^2 d\tau$$

where  $h_{\text{init}}$  is the initial altitude of the UAV;  $t_0$  and  $t_n$  are the transition start and end times.

### (2) Safety margin optimization

The target flight trajectory ensures the maximum safety margin for the UAV during flight, thus the discrepancy between the optimal flight trajectory and the target flight trajectory must be taken into account in the design process. In this paper, an optimization objective function for the flight trajectory safety margin is established as:

$$J_2 = \int_{v_0}^{v_n} (\theta(V) - \theta^*(V))^2 dV$$

where  $\theta(V)$  is the actual flight trajectory;  $\theta^*(V)$  is the target flight trajectory;  $v_0$  and  $v_n$  are the UAV speeds at the beginning and end.

### (3) Actuator margin optimization

The lower the actuator output necessary for UAV flight maneuvering, the greater the available output of the remaining actuators for maneuvering and attitude control. Consequently, this paper formulates an actuator margin optimization objective as:

$$J_3 = \int_{t_0}^{t_n} \left( \left( \frac{\omega(\tau)}{\omega_{\text{max}}} \right)^2 + \left( \frac{\delta_e(\tau)}{\delta_{e,\text{max}}} \right)^2 \right) d\tau$$

where  $\omega(\tau)$  is the propeller speed;  $\omega_{\text{max}}$  is the maximum speed of the propeller;  $\delta_e(\tau)$  is the rudder angle;  $\delta_{e,\text{max}}$  is the maximum rudder deflection angle.

### (4) Control effect optimization

When the UAV embarks on a flight mission, it must take into account the feasibility of its trajectory. In order to minimize the discrepancy between the actual state and the desired state, this paper establishes an optimization objective function for the flight control effect, which is formulated as:

$$J_4 = \omega_u \cdot (u(t_n) - u_n)^2 + \omega_w \cdot (w(t_n) - w_n)^2 + \omega_\theta \cdot (\theta(t_n) - \theta_n)^2$$

where  $\theta$  is the pitch angle;  $u$  and  $w$  are the velocities along the  $x^B$  and  $z^B$  axes under the body. Combining the above analysis, the final optimization objective cost function  $J$  is:

$$J = k_1J_1 + k_2J_2 + k_3J_3 + J_4 = k_1J_1 + k_2J_2 + k_3J_3 + \omega_u \cdot (u(t_n) - u_n)^2 + \omega_w \cdot (w(t_n) - w_n)^2 + \omega_\theta \cdot (\theta(t_n) - \theta_n)^2$$

where  $k_1, k_2, k_3, \omega_u, \omega_w$  and  $\omega_\theta$  are the weighting coefficients.

### 8. Flight Test

This section describes the flight experiments conducted on three tail-sitter VTOL UAV scaled-down prototypes, one with and one without free-tail technology incorporated, as depicted in Figure 22, UAV image of a ground-level elevation shot in conventional weather.

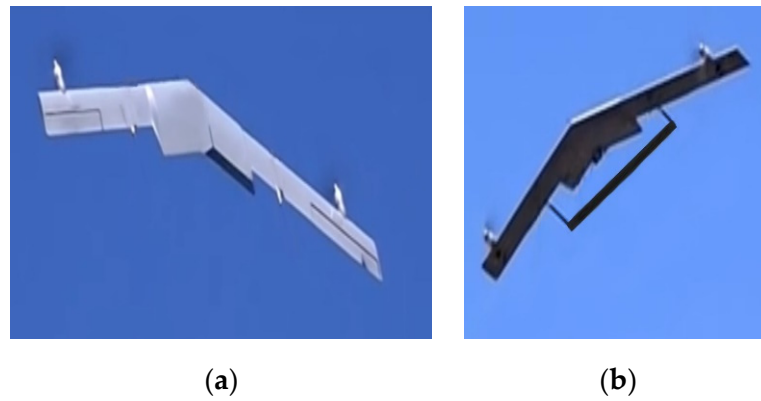


Figure 22. Flight test (a) without a free-tail; (b) with a free tail.

The integration of the free tail into the UAV design is primarily aimed at augmenting the pitch control capability. Therefore, the experiments conducted in this study predominantly focus on comparing the UAV’s performance during transition and cruise states. The comparison entails analyzing the pitch tracking curve, peak pitch angle rate, and rate of change through flight tests executed along a rectangular trajectory at altitudes ranging from 100 to 300 m, as illustrated in Figure 23.

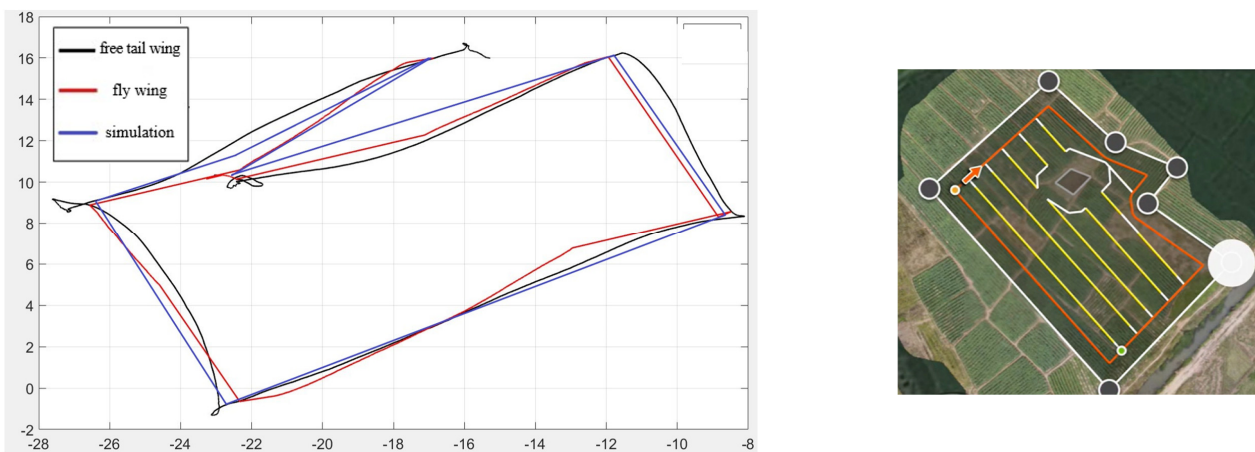
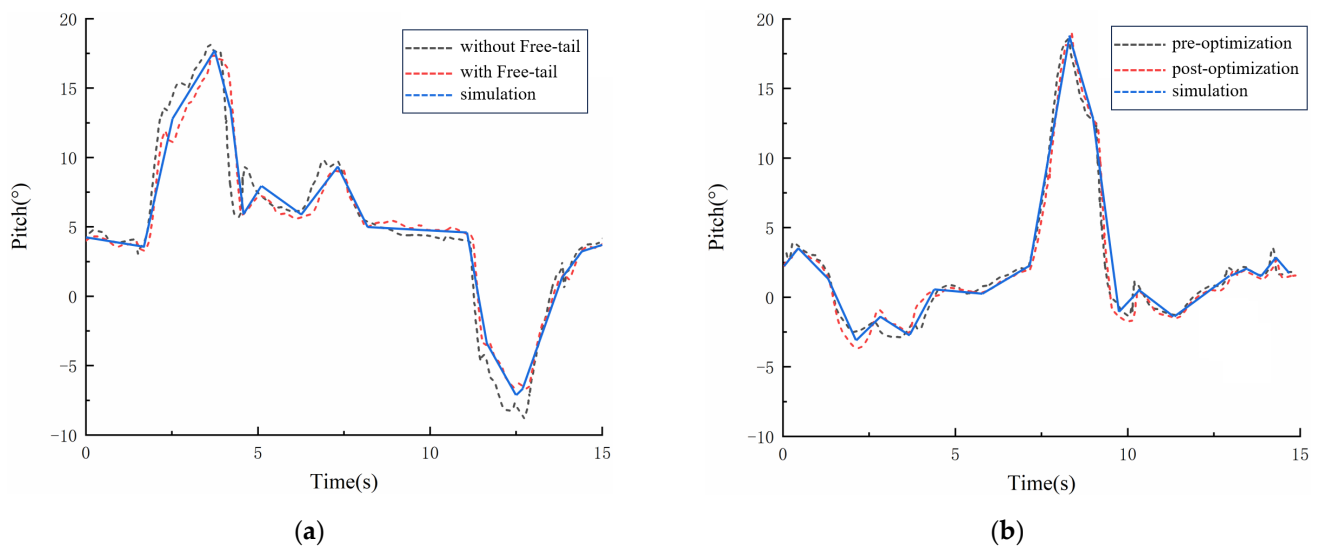
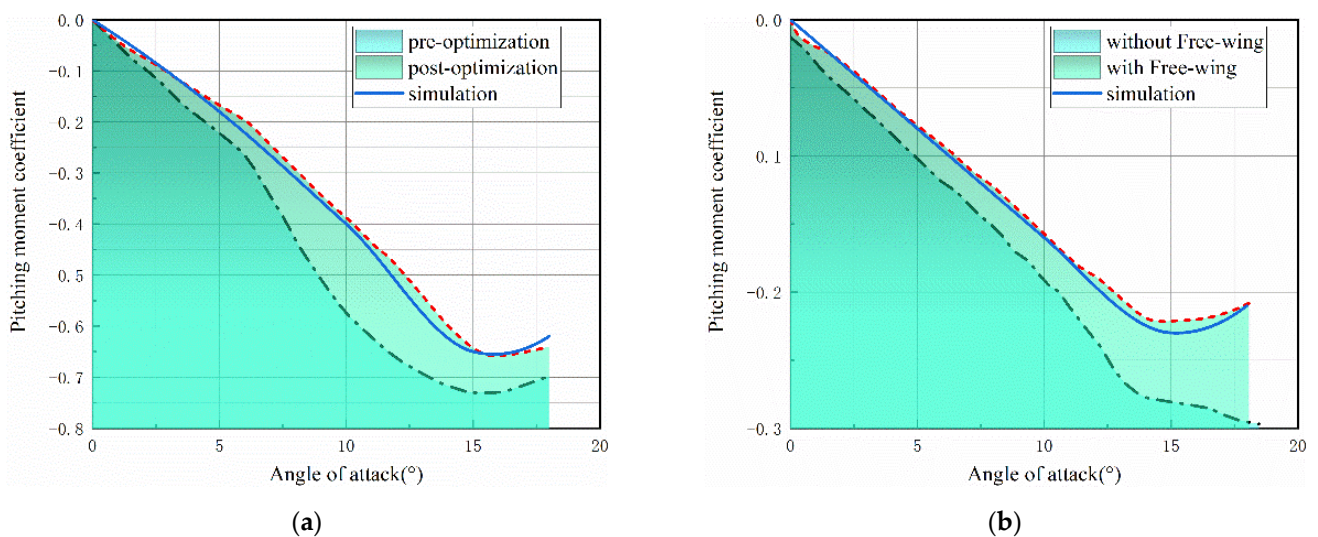


Figure 23. Flight path. The red arrow represents the direction of drone operation, the white line and dots represent the target cruising area of the drone, and the yellow line represents the trajectory that has not been operated to.

Figures 24 and 25 clearly demonstrates that the utilization of free-tail technology and the optimization of 4–6 knots substantially improve control performance and longitudinal stability when compared to the flying wing configuration.



**Figure 24.** Comparison of pitch tracking (a) between with/without a free tail and simulation. (b) between pre/post-optimization and simulation with a free tail.



**Figure 25.** Comparison of pitch moment coefficient. (a) Full Fuselage between pre/post-optimization and simulation with a free tail. (b) Horizontal tail between with/without a free tail and simulation.

In the lateral dynamics of conventional tailless configurations, a notable coupling exists between roll and yaw. The simulation results presented in Figure 26 enable us to compare the peak yaw angular rate and its rate of change between two distinct configurations: one featuring a thrust vectoring rotor and the other incorporating a vertical tail into the free tail. It is evident that the difference in yaw maneuverability and agility between these two setups is not substantial. Nonetheless, it should be emphasized that the tail-sitter VTOL UAV and conventional fixed-wing aircraft both employ a rudder during the approach phase. Consequently, no specific investigation was conducted on the relevant characteristics of the vertical tail in this study.

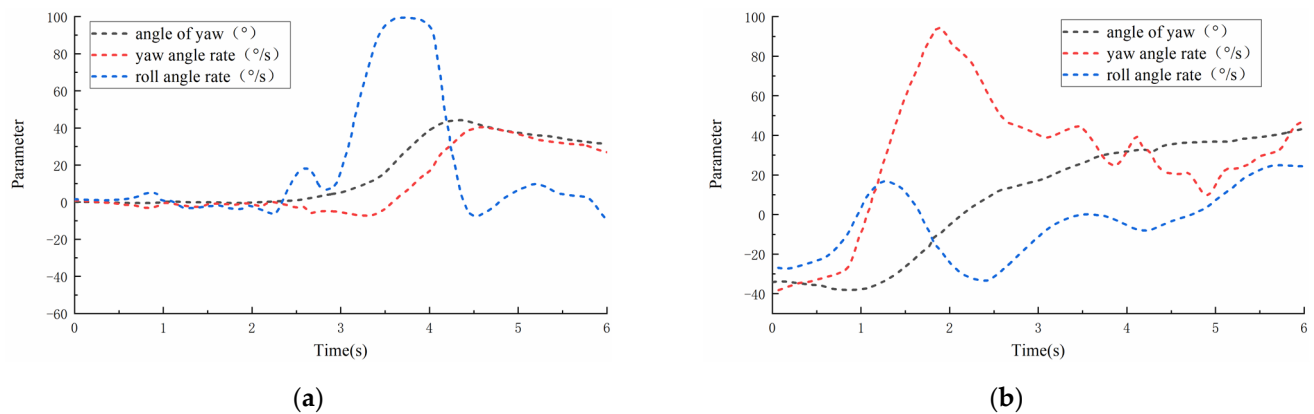


**Figure 26.** Transverse characteristics of flight simulation (a) with drooping tail; (b) using a thrust vector.

Finally, the unique capability of tail-sitter VTOL UAVs to perform narrow-area takeoff and landing, as well as their synergistic interaction with ring-side crops during shuttle flights, as illustrated in Figures 27 and 28, will be the focal point of the subsequent phase of this research, building upon the findings presented in this paper. Furthermore, the investigation of free-tail-based terrain adaptive takeoffs and landings will also be incorporated into this future study.



**Figure 27.** Tail-sitter VTOL UAV crop gap narrow-area takeoff.



**Figure 28.** Adaptive landing simulation tail-sitter VTOL UAV with a free tail.

## 9. Discussion

The agricultural tail-sitter VTOL UAV is characterized by its stringent demands on flight stability and terrain adaptability due to the intricate operating environment and expansive operational area. In response to these challenges, this paper presents a comprehensive technical solution for the tail-sitter VTOL UAV, which is based on the free-tail configuration. The proposed solution enables dual-mode operation for landing and cruising by employing the landing gear in two distinct manners. Specifically, the structure of

the free tail serves as an adaptive landing gear during takeoff and landing, allowing the tail-sitter VTOL UAV to operate on non-planar terrains such as slopes, mountains, and terraces. This feature effectively enhances the terrain adaptability of the tail-sitter VTOL UAV and improves its landing stability in the VTOL state. Furthermore, the presence of the free tail enables the tail-sitter VTOL UAV to transition from a flying wing layout to a double tail strut layout during cruise, thereby significantly enhancing its stability. As the connecting structure of the double tail strut layout, the free tail effectively minimizes the extra drag generated by its own structure while increasing the size of the tail structure. Compared to the traditional tail-sitter UAV configurations mentioned in references [4,6–12]. This solution addresses the issue of poor stability at low speeds inherent in conventional tailless tail-sitter VTOL UAV designs.

## 10. Conclusions

(1) In order to optimize the performance of the free tail, this paper investigates the impact of various layout parameters on the flight performance of a tail-sitter VTOL UAV through numerical calculations based on the SST  $k$ - $\omega$  model. Specifically, this study delves into the aerodynamic coupling between the rotor propeller, wing, and free tail during cruise, as well as the influence of landing gear attitude on hovering stability and ground effect in the VTOL state.

(2) This paper scrutinizes the boundary conditions that encompass the transition state. The layout characteristics affecting the flight performance of the tail-sitter VTOL UAV are comprehensively summarized, and the free-tail layout form is ultimately determined through multi-objective optimization under multi-modal conditions.

(3) Through a comparison with the simulation of a scaled-down prototype in a flight test machine, it is substantiated that the adoption of a free-tail structure is advantageous and practical. The optimization method employed can significantly enhance the stability capability and flight efficiency of the tail-sitter VTOL UAV. Consequently, future research will focus on investigating the coupling efficacy between the tail-sitter VTOL UAV and the surrounding crop during narrow-area flight, as well as its terrain adaptive takeoff and landing performance. This endeavor will contribute to advancing the application of the tail-sitter VTOL UAV in the agricultural domain.

**Author Contributions:** Conceptualization, H.Q.; Methodology, H.Q.; Software, H.Q.; Validation, S.-J.C.; Formal analysis, S.-J.C.; Investigation, S.-J.C.; Resources, J.-Y.W.; Data curation, J.-Y.W.; Writing—original draft, Y.-M.P.; Writing—review & editing, Y.-M.P.; Visualization, H.N.; Supervision, H.N.; Project administration, X.-H.W.; Funding acquisition, X.-H.W. All authors have read and agreed to the published version of the manuscript.

**Funding:** The research was funded by the National Defense Outstanding Youth Science Foundation grant number 2018-JCJQ-ZQ-053 funded by Xiaohui Wei, the National Natural Science Foundation of China grant number 52202441 and the Natural Science Foundation of Jiangsu Province grant number BK20220910 funded by Yiming Peng, and the Priority Academic Program Development of Jiangsu Higher Education Institutions. The authors would also like to thank the anonymous reviewers, associate editor, and editor for their valuable and constructive comments and suggestions.

**Data Availability Statement:** Data available on request due to privacy. The data presented in this study are available on request from the corresponding author due to privacy.

**Conflicts of Interest:** The corresponding author states that there is no conflict of interest.

## References

1. Alwateer, M.; Lokes, W. Emerging Drone Services: Challenges and Societal Issues. *IEEE Technol. Soc. Mag.* **2020**, *39*, 47–51. [[CrossRef](#)]
2. Kubo, D.; Suzuki, S. Tail-Sitter VTOL Unmanned Aerial Vehicle: Transitional Flight Analysis. *J. Aircr.* **2012**, *45*, 292–297. [[CrossRef](#)]
3. Tang, W.; Song, B.F. Transitional flight equilibrium and performance study for the X-NMRL tail-sitter VTOL MAV. *Proc. Inst. Mech. Eng. Part G J. Aerosp. Eng.* **2018**, *233*, 095441001879473. [[CrossRef](#)]

4. Wang, K.; Ke, Y.; Chen, B.M. Autonomous reconfigurable hybrid Tail-sitter VTOL UAV U-Lion. *Sci. China Inf. Sci.* **2017**, *60*, 1–16. [[CrossRef](#)]
5. Ang, K.Z.; Cui, J.Q.; Pang, T.; Li, K.; Wang, K.; Ke, Y.; Chen, B.M. Design and Implementation of a Thrust-Vectored Unmanned Tail-Sitter with Reconfigurable Wings. *Unmanned Syst.* **2015**, *3*, 143–162. [[CrossRef](#)]
6. Leon, B.L.; Rimoli, J.J.; Leo, C. Rotorcraft Dynamic Platform Landings Using Robotic Landing Gear. *J. Dyn. Syst. Meas. Control.* **2021**, *143*, 111006. [[CrossRef](#)]
7. Roderick, W.; Cutkosky, M.; Lentink, D. Bird-inspired dynamic grasping and perching in arboreal environments. *Sci. Robot.* **2021**, *6*, eabj7562. [[CrossRef](#)]
8. Liu, J.; Zhang, D.; Wu, C.; Tang, H.; Tian, C. A multi-finger robot system for adaptive landing gear and aerial manipulation. *Robot. Auton. Syst.* **2021**, *146*, 103878. [[CrossRef](#)]
9. Ding, Z.; Wu, H.; Wang, C.; Ding, J. Hierarchical Optimization of Landing Performance for Lander with Adaptive Landing Gear. *Chin. J. Mech. Eng.* **2019**, *32*, 1–12. [[CrossRef](#)]
10. Tang, H.; Zhang, D.; Tian, C. A method for comprehensive performance optimization of four-leg landing gear based on the virtual equivalent parallel mechanism. *Mech. Mach. Theory* **2022**, *174*, 104924. [[CrossRef](#)]
11. Li, H.; Li, C.; Li, H.; Li, Y.; Xing, Z. An Integrated Altitude Control Design for a Tail-sitter VTOL UAV Equipped with Turbine Engines. *IEEE Access* **2017**, *5*, 10941–10952. [[CrossRef](#)]
12. Kuang, M.; Zhu, J.; Wang, W.; Tang, Y. Flight controller design and demonstration of a thrust-vectored tailsitter. In Proceedings of the 2017 IEEE International Conference on Robotics and Automation (ICRA), Singapore, 29 May–3 June 2017; IEEE: Piscataway, NJ, USA, 2017.
13. Zhong, J.; Wang, C. Transition characteristics for a small tail-sitter unmanned aerial vehicle. *Chin. J. Aeronaut.* **2021**, *34*, 220–236. [[CrossRef](#)]
14. Bousquet, J.M.; Gardarein, P. Improvements on Computations of High Speed Propeller Unsteady Aerodynamics. *Aerosp. Sci. Technol.* **2003**, *7*, 465–472. [[CrossRef](#)]
15. Roosenboom, E.; Stuermer, A.; Schröder, A. Advanced Experimental and Numerical Validation and Analysis of Propeller Slipstream Flows. *J. Aircr.* **2010**, *47*, 284–291. [[CrossRef](#)]
16. Chen, H.R.; Wang, X. General Modeling Algorithm for Propeller Mathematical Model Based on Component Characteristics. *J. Propuls. Technol.* **2019**, *40*, 1681–1692. (In Chinese)
17. Xu, H.Y.; Ye, Z.Y. Numerical simulation of unsteady propeller slipstream. *J. Aerosp. Power* **2011**, *26*, 148–153. (In Chinese)
18. Shi, W.B.; Li, J. Numerical simulation of contra-rotating propeller flowfield aerodynamic interactions. *J. Aerosp. Power* **2019**, *34*, 829–837. (In Chinese)
19. Yang, X.C.; Wang, Y.T.; Meng, D.H.; Tao, M.; Wei, W. Study on wing slipstream effects of distributed propellers with different rotating directions. *Acta Aerodyn. Sin.* **2019**, *37*, 89–98. (In Chinese)
20. Chen, H.R.; Wang, X. A modeling method of propeller based on the propeller component characteristic. *J. Aerosp. Power* **2017**, *32*, 2526–2535. (In Chinese)
21. Xia, Z.F.; Yang, Y. Unsteady Numerical Simulation of Interaction Effects of Propeller and Wing. *Acta Aeronaut. Astronaut. Sin.* **2011**, *32*, 1195–1201. (In Chinese)
22. Zhang, G.Q.; Yang, S.X. Experimental investigation of the aerodynamic characteristics of tandem-airfoil based on low Reynolds number. *Chin. J. Comput. Mech.* **2010**, *27*, 733–737.
23. Sudhakar, S.; Chandankumar, A.; Venkatakrishnan, L. Influence of Propeller Slipstream on Vortex Flow Field over a Typical Micro Air Vehicle. *Aeronaut. J.* **2017**, *121*, 95–113. [[CrossRef](#)]
24. Sarkisov, Y.S.; Yashin, G.A.; Tsykunov, E.V.; Tsetserukou, D. DroneGear: A Novel Robotic Landing Gear with Embedded Optical Torque Sensors for Safe Multicopter Landing on an Uneven Surface. *IEEE Robot. Autom. Lett.* **2018**, *3*, 1912–1917. [[CrossRef](#)]
25. Hu, D.; Li, Y.; Xu, M.; Tang, Z. Research on UAV Adaptive Landing Gear Control System. *J. Phys. Conf.* **2018**, *1061*, 012019. [[CrossRef](#)]
26. Zhu, X.; Zheng, G.; Hou, Z. Solar-powered airplanes: A historical perspective and future challenges. *Prog. Aerosp. Sci.* **2014**, *71*, 36–53. [[CrossRef](#)]
27. Menter, F.; Rumsey, C. Assessment of Two-Equation Turbulence Models for Transonic Flows. In Proceedings of the AIAA, Springs, CO, USA, 20–23 June 1994.
28. Bravo-Mosquera, P.D.; Botero-Bolivar, L.; Acevedo-Giraldo, D.; Cerón-Muñoz, H.D. Aerodynamic design analysis of a UAV for superficial research of volcanic environments. *Aerosp. Sci. Technol.* **2017**, *70*, 600–614. [[CrossRef](#)]
29. Theys, B.; Dimitriadis, G.; Andrianne, T.; Hendrick, P.; De Schutter, J. Wind Tunnel Testing of a VTOL MAV Propeller in Tilted Operating Mode. In Proceedings of the 2014 International Conference on Unmanned Aircraft Systems (ICUAS), Orlando, FL, USA, 27–30 May 2014.
30. Khan, W.; Nahon, M. A Propeller Model for General Forward Flight Conditions. *Int. J. Intell. Unmanned Syst.* **2015**, *3*, 72–92. [[CrossRef](#)]

**Disclaimer/Publisher’s Note:** The statements, opinions and data contained in all publications are solely those of the individual author(s) and contributor(s) and not of MDPI and/or the editor(s). MDPI and/or the editor(s) disclaim responsibility for any injury to people or property resulting from any ideas, methods, instructions or products referred to in the content.